Characterisation of Geometric Accuracy in Metal Fused Filament Fabricated Parts Using X-ray Computed Tomography

Available online at www.sciencedirect.com

ScienceDirect

Procedia CIRP 139 (2026) 343–348

www.elsevier.com/locate/procedia

13th CIRP Global Web Conference (CIRPe 2025)

Characterisation of Geometric Accuracy in Metal Fused Filament Fabricated Parts Using X-ray Computed Tomography

Roham Sadeghi Tabar*[a,b], Andi Kuswoyo[b,c], Christos Margadji[b], Sebastian W. Pattinson[b]

[a] *Chalmers University of Technology, SE-41296 Gothenburg , Sweden*

[b] *Department of Engineering, University of Cambridge, Trumpington Street, Cambridge CB2 1PZ, UK*

[c] *Faculty of Mechanical and Aerospace Engineering, Institut Teknologi Bandung, Jl. Ganesha 10, Bandung 40132, Indonesia*

* Roham Sadeghi Tabar. Tel.: +46-031-772-6745. *E-mail address:* rohams@chalmers.se

Abstract

This work presents a methodology for quantifying geometric deviations in metal parts fabricated via Fused Filament Fabrication (FFF) using Ultrafuse 316L stainless steel filament. A blade-shaped geometry is selected as a representative case and analysed before and after sintering using high-resolution X-ray computed tomography (XCT). The XCT data are aligned to nominal and scaled geometries to assess deviations introduced during each manufacturing stage. In parallel, a thermo-mechanical sintering simulation is performed to predict shrinkage and deformation. Comparison between simulated results and XCT data reveals location-dependent discrepancies, with deformation at critical regions exceeding 2 mm and simulation errors ranging from 0.5 to 2 mm. The study highlights the limitations of standard shrinkage scaling and demonstrates the value of XCT-based characterisation in validating and improving predictive models for metal FFF. The proposed approach provides a foundation for model-informed design and process compensation strategies in sintering-based additive manufacturing.

Keywords: Metal Additive Manufacturing; Defect Classification; AI; Quality Control

1. Introduction

Additive Manufacturing (AM) is a manufacturing method that adds material layer by layer to create a part, unlike the traditional subtractive approaches, i.e., cutting. This approach has gained significant attention in the 2010s due to the design flexibility that it provides [1]. Several categories of additive processes have been traditionally identified, while the application of binder jetting [2], directed energy deposition [3], material extrusion [4], and powder bed fusion [5] have been widespread. The diverse available AM methods make the fabrication of almost all types of mechanical products accessible. However, there are still challenges associated with AM, which are limiting the AM potential *i.e.*, constraints in upscaling and quality concerns that necessitate post-processing [6]. Furthermore, the layer-by-layer deposition process in AM is highly prone to geometric variations, primarily due to thermal effects associated with heating and cooling cycles. As a result, quality control in AM has become a critical area of intensive research and development [6, 7].

1.1. Fused filament fabrication

Among contemporary AM processes, fused filament fabrication (FFF) has established itself as the predominant technology, supporting a wide range of applications across manufacturing sectors, including biomedical, aerospace, automotive, and many others [8, 9]. While providing design freedom, FFF is cost-effective, leading to a large share in additive manufacturing [8]. In the FFF domain, previous studies have introduced an infrared-based system for high-resolution, in-process thermal monitoring of the process and validates it against a dedicated numerical models [10].Furtheremore, a temperature-based criterion to predict FFF printing failures caused by insufficient cooling and generalizable to other materials for adaptive printing strategies has been introduced [11]. Recent advances in metal-filled filaments now allow stainless-steel printing on unmodified desktop FFF machines, i.e., UltraFuse 316, which combines standard FFF shaping with conventional debinding and sintering [12]. One of the primary limitations of 316 L

2212-8271
10.1016/j.procir.2025.09.045

stainless-steel FFF is part size. Previous research has demonstrated that this constraint extends into post-processing of parts with wall thicknesses above 4 mm, developing cracks and other defects during debinding and sintering [13]. Due to the two-step process of metal FFF, the parts are prone to extreme dimensional changes, as the parts shrink during the debinding and sintering. In addition, the heating and cooling cycles, combined with the fusion of metal particles during sintering, can introduce further deformation, often influenced by the geometry and design of the part. A multitude of variables, including filament composition, print settings, and post-processing protocols, strongly affect final part geometric accuracy. To drive broader industrial adoption, both hardware and software refinements are necessary, with a particular emphasis on interlayer bonding. For example, preheating each deposited layer immediately before the next extrusion has been shown to improve adhesion and reduce delamination significantly [14]. In the next section, the details associated with the geometric accuracy of the FFF of metal parts, the focus of this study, are presented.

1.2. Geometric accuracy in Metal FFF

Sintering-induced shrinkage represents a critical challenge in FFF-based metal part fabrication. To compensate, printed geometries are typically oversized by applying a uniform scaling factor to the nominal geometry [15], but shrinkage in practice is anisotropic [16]. Previous studies have shown that printing with the 316L stainless steel filament yields parts with 13–18% shrinkage in the X–Y plane and 15–23% shrinkage along Z [17]. However, estimating the shrinkage factor prior to printing is a challenge that requires trial and error based on the geometric features of the component to be printed. To compensate for the errors, previous studies have focused on physics-informed approaches to compensate for the existing error during the process on the individual part [18] and batch level [19]. Other sources of deviations may occur due to the applied printing parameters, *i.e.*, the layers' direction, layer thickness, and infill pattern. The thermal deviation associated with FFF is essentially different from other heat-induced deformations in other processes, *i.e.*, DED, which can be seen as a welding process [7]. While in these processes the parts will undergo phase change, due to material melting, the expected deformation due to heat is larger [20, 21]. In FFF of metals, after printing the parts undergo solid state diffusion during the sintering at a temperature up to 1400°C. Increasing the temperature during this phase can reduce the sintering hold time but also result in large distortion [14]. To quantify the dimensional changes in FFF of metals, shrinkage and angle variation in overhang pillars using analytical modeling, finite-element simulation, and experiments that account for gravity induced bending have been studied [16]. In this study, the geometric accuracy of the metal FFF is further investigated and evaluated.

1.3. Scope of the paper

Metal FFF provides exceptional advantages in the design and manufacturing of complex geometries. This method is associated with considerable geometrical changes during the printing, debinding, and sintering, imposing geometrical uncertainty on the final geometry. In this study, we leverage X-ray computed tomography (XCT) scans of stainless steel 316L FFF parts before and after sintering to quantify the actual geometric deviation and compare the result to a displacement predicted by a sintering simulation. The rest of the paper is structured as follows. Section 2 provides the experimental approach, presents the selected reference case for this study, and describes the implementation of the approach. Section 3 presents the results and discussions of these and is followed by a conclusion in Section 4.

2. Method

To evaluate the geometry deviation after the sintering process, a representative geometry has been selected, and the XCT data have been gathered at each step of the process, after printing and after sintering. The printing properties have been experimented on to achieve acceptable layer adhesion and to achieve less first-layer separation. After registering the final deviation after sintering, a simulation of the sintering process is performed to further compare the shrinkage achieved through a theoretical model and the XCT data. Fig. 1 shows a schematic view of the approach taken in this study.

2.1. Reference case

The reference case in this study is a blade shape with a trapezoidal base. The case is chosen because of the complex curvature that is prone to deviation during the heat-imposed process. The dimension of the reference case has been 18 mm in the X-direction, 14.7 mm in the Y-direction, and finally 22.7 mm in the Z-direction. Fig. 2 visualises the reference case and the dimensions. As visualised, the blade is changing direction in 2 dimensions, making the curvature complex to model in one step.

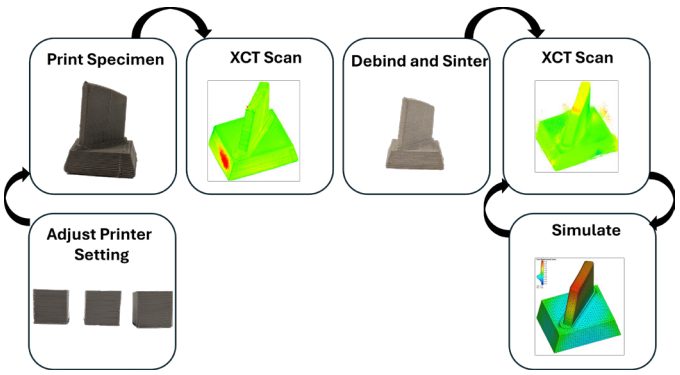

Fig. 1. The framework of the geometry analysis of the metal FFF with XCT data

2.2. Material and printing parameters

The filament used for the experiments is BASF Ultrafuse 316L, a metal-polymer composite filament comprising 316L stainless-steel powder dispersed in a thermoplastic binder matrix. Supplied in 1.75 mm nominal diameter, the filament contains approximately 80% by weight stainless-steel loading, yielding a green part that can be processed via standard FFF hardware [22]. Prior to printing, the filament spool is positioned on a spool feeder with a bearing to avoid underextrusion. Slicing was performed in Ultimaker Cura V5.9. Printing trials are conducted on an unmodified desktop FFF printer, Creality Ender 3 Pro, equipped with a hardened-steel nozzle 0.4 mm in diameter to resist abrasive wear. Fig. 3 visualises the outcomes of the single wall cube test for the different print settings. The two figures on the left clearly visualize the layer separation for lower print speed at 25 mm/s and lower hot end temperature at 250 and 255°C, respectively. The dimension of the test cube is 20 mm. and the infill for the test has been 100%. The hot end is set to 260°C, and the build plate is heated to 120°C. Print speed is set to 35 mm/s, and a layer height of 0.2 mm is selected to balance surface quality and dimensional stability. To avoid first-layer delamination, a raft is used during the slicing as a build plate adhesion type, and the wall thickness is set to 1.2 mm to avoid layer separation. After each build, green parts are carefully removed and visually inspected for consistent extrusion, absence of under-extrusion, and complete interlayer fusion before proceeding to debinding and sintering. A single-wall cube test has been performed to observe the outcome of the printing and to approach the above-stated parameters. A flow rate calibration value has been achieved as a result of these tests, and this value has been set to 106%. It is worth noting that the hot-end and build plate temperatures exceed the recommended values, primarily due to discrepancies between the machine environment and the actual printing and build plate temperatures.

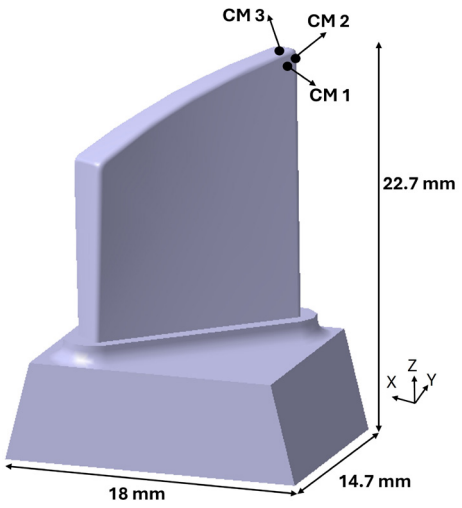

Fig. 2. The reference case and the corresponding dimensions

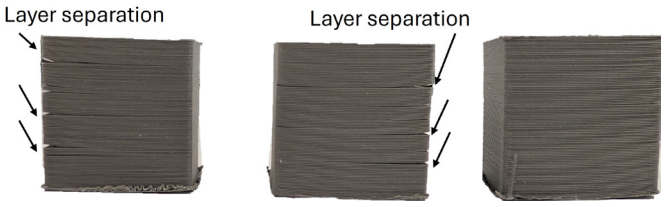

Fig. 3. Layer separation for different print settings (First and second from left) and the adjusted setting (on the right). The cube dimension is 20 mm and the print parameters are specified in Section 2.2

The reference case in this study has been printed with the calibrated settings specified and 100% infill rate.

2.3. X-ray Computed Tomography and simulation strategy

A Nikon X Tek 225 H micro–CT system (2880 × 2880-pixel detector) is employed to acquire volumetric data of the blade geometries. The specimen is mounted on a base with foam material and scanned in two sessions, one after printing and one after sintering the specimen. The raw axial projections are reconstructed into a 3D voxel volume using the 3D Slicer software [23]. To isolate the metal parts from the foam, an automatic intensity threshold is utilised to remove low-density voxels, then a median smoothing filter is used to suppress residual geometries. Finally, the volumes are segmented into separate volumes, each recentered into its own coordinate system, for individual analysis. The reconstructed geometries are then postprocessed, and the remaining outlier points are filtered from the geometries manually. The resulting geometries are then roughly aligned to the nominal geometry and finally registered with the Iterative Closest Point (ICP) in the software CloudCompare [24]. The mesh distances are also computed for each step before and after sintering, and the colourplot is utilised to visualise the deviation, Fig. 1.

To simulate the outcome of the sintering on the nominal geometry, the commercial software Simufact Additive is utilised, taking into account the sintering stress, effective bulk and shear viscosity, and grain growth. Based on these parameters, the elastic, thermal, and visco-plastic strains result. The initial relative density is set to 62% to represent the typical solid fraction of debound parts, consistent with random close packing of the powders yielding realistic sintering shrinkage predictions. This value is set to match the predicted densification kinetics to the measured dilatometry shrinkage data. The mesh size 0.5 mm tetrahedra defined with automatic meshing functions. The sintering temperature has been in the range of 20 to 1380°C, and the hold time at maximum temperature has been three hours. The detailed sintering cycle has been visualized in Fig4. The sintering schedule comprises heating from 20°C with isothermal holds at 300°C, 17000 to 19000 s, and 450°C, 28000-31500 s, followed by a ramp to a peak hold at 1385°C, 42500–53500 s, and subsequent cooling to 20°C at 70,000 s. This 0–70,000 s time–temperature profile was used as the thermal boundary condition in the simulations to reproduce the experimental thermal history, densification, and shrinkage. Postprocess-

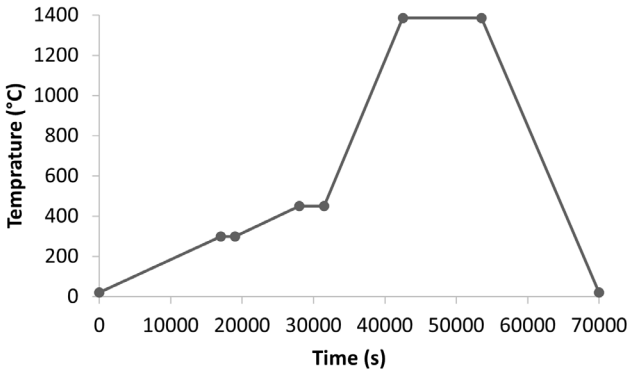

Fig. 4. The thermal sintering cycle

ing included von Mises patterns reported as region averaged over a 0.5 mm neighborhood to avoid mesh singular peaks and nodal displacements. The resulting thermo-mechanical stress is achieved, and the displacements are then calculated using FEM. The outcome is post-processed and visualised in a colourplot, Fig. 1.

3. Results

The blade geometry is successfully printed on the desktop printer with the specified printer settings and 100% infill rate, Section 2. The printed part is scanned with XCT with the specified scanning setup. The resulting geometric deviation from the nominal geometry is visualised in Fig. 5. The range of the deviation after printing is predominantly within the range ±0.2 mm, with a mean value of 0.1 mm in the surface normal direction. Later, the part is debound and sintered, and XCT data after sintering is gathered and reconstructed into a 3D volume. For comparing the outcome of the sintered part, the nominal geometry is shrunk based on the material provider's design guidelines as 16% in X and Y-directions and 20% in the Z direction. The two geometries are then aligned, and deviation is registered. The outcome of this step is visualised in Fig. 6. The range of the deviation after sintering is predominantly $-1/+2$ mm, with a mean value at 0.3 mm in the normal direction.

The nominal blade geometry after sintering is also simulated to compare the overall displacement and compliance with the design guidelines and the achieved geometry after sintering. The simulated blade after sintering is visualised in Fig. 7. The range of the displacements here is from 0.1 to 3.26 mm, with a mean value of 0.99 mm. The resulting stresses after sintering are also evaluated and visualised in Fig. 8. The critical zone of stress is at the base of the blade where the stresses are up to 2.23 *kPa*. The maximum local peak stresses are near the geometric transitions on the base and blade intersection at 41.68 *kPa*.

To further evaluate the displacement of the reference case, three critical measures (CM 1-3) at the tip of the blade are considered in three surfaces, in the surface normal direction. These measures are chosen due to the functionality of the blade and the sensitivity to the deviation in this area. Considering this area shown in Fig. 2, the displacements at each critical point are presented in Table 1. For CM 1, the simulated result deviates substantially from the XCT measurement after sintering, with an error of approximately 2.3 mm relative to the scaled geometry. For CM 2, the simulated displacement exceeds the XCT displacement by about 1 mm, indicating a closer agreement and an improved predictive capability compared to the experiment. A similar trend is observed for CM 3, where the difference between the scaled simulated displacement and the XCT deviation of the sintered blade is reduced to approximately 0.5 mm.

One other aspect that is captured in the XCT data is the existence of warpage on the base of the blade, which could result in higher displacements than the simulated data. Furthermore, other geometrical effects, *i.e.*, bulges due to excessive material extrusion or seam line on the tool path direction exist in the XCT data of the sintered part, see Fig. 6 at the top of the blade, that further contribute to the discrepancies in the simulated data and the XCT data, .

The reference case before and after debinding and sintering is visualized in Fig. 9.Label (A) is the side view of the parts. In (B), the measurments in length and width are presented. In (C), The height of the reference case before and after sintering is measured and visualized. As can be seen shrinkage occurs predominantly in the height in (C) and (A). This also agrees with the results of the XCT data, but also the simulation. In the length and width of the specimen, this shrinkage is also clearly noticable in (B).

The evaluation of the results indicates that local deviations are primarily concentrated at the blade tip and base. At the base, the relatively large mass leads to stress accumulation, resulting in measurable out-of-plane distortion and warpage. At the blade tip, the complex geometric transition associated with the rota-

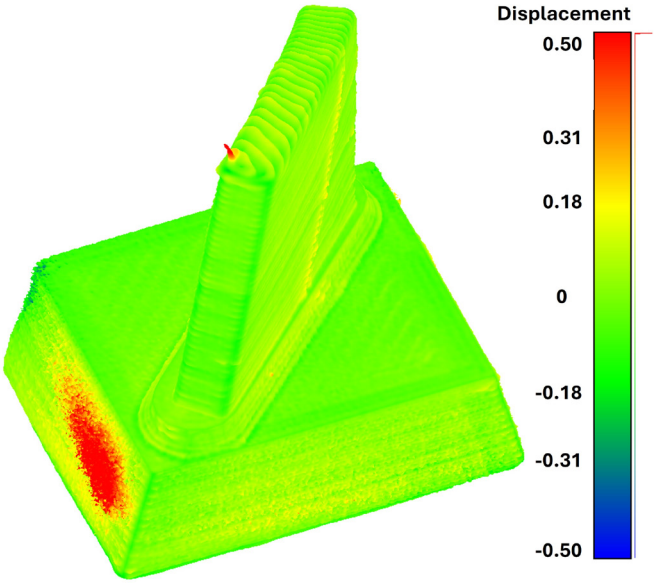

Fig. 5. XCT reconstructed data before sintering compared to the nominal geometry

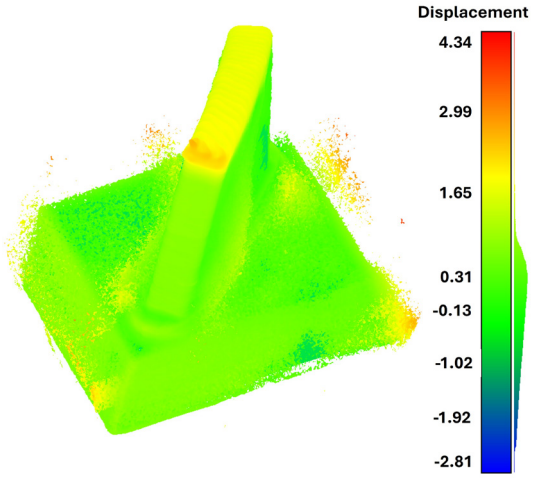

Fig. 6. XCT reconstructed data after sintering compared to the scaled geometry, shrunk based on design guidelines

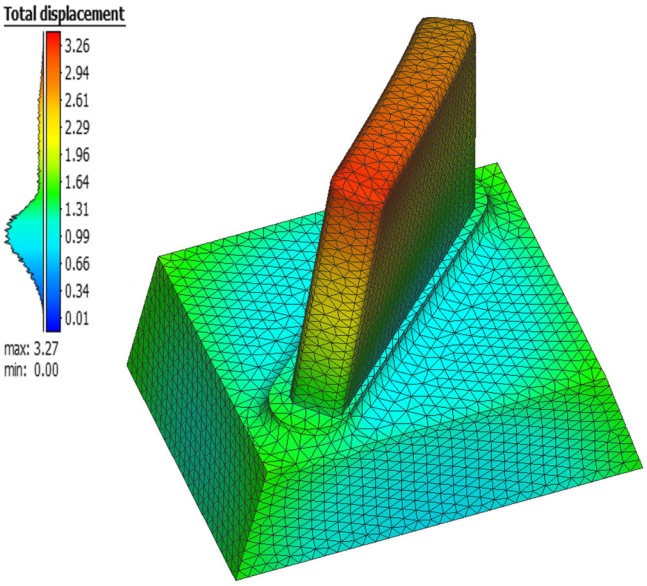

Fig. 7. Simulated displacement of nominal blade after sintering

Table 1. Geometric displacement at the critical measures

Critical Measure	Displacements (mm)			
	Pre-Sinter Scan	Post-Sinter Scan	Simulated	
	From nominal	From scaled	From nominal	From scaled
CM 1	0.07	0.32	3.18	2.67
CM 2	0.11	1.68	3.13	2.62
CM 3	0.17	2.15	3.26	2.61

Scaling factor has been 16% for X and Y directorin, and 20% for Z direction

tion along the Z- and X-axes makes the prediction of displacement more challenging. Moreover, the results demonstrate that isotropic scaling provides a useful baseline; however, it fails to capture location-dependent shrinkage gradients and constraint-induced warpage.

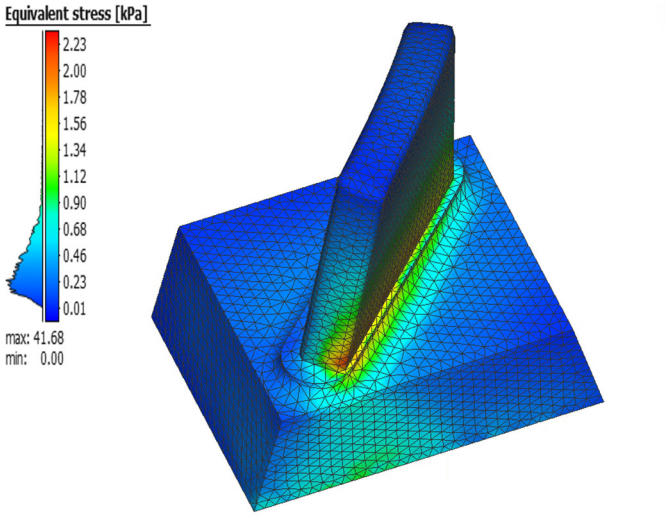

Fig. 8. Simulated stress of nominal blade after sintering

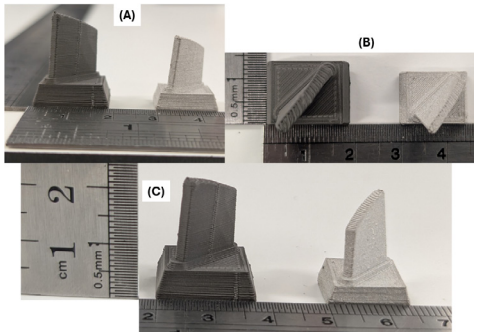

Fig. 9. Reference case before debinding and sintering (DS), left specimen in (A), (B) and (C), and after DS, right specimen in (A), (B) and (C) measured in different views.

4. Conclusion

This study presents a comprehensive methodology for characterising geometric deviations in metal FFF parts using X-ray computed tomography (XCT), with a focus on Ultrafuse 316L stainless steel. By analysing a representative blade geometry, deviations before and after sintering are quantified and compared to predictions from a thermo-mechanical sintering simulation. The XCT results reveal that the printed green parts exhibit minimal deviation from the nominal geometry, with a mean deviation of approximately 0.1 mm. However, after sintering, the deviation increases significantly by up to 2 mm in some areas, highlighting the impact of thermal shrinkage and stress-induced deformation. The simulation predicted overall deformation trends with reasonable accuracy at critical locations with mainly Z-dominant direction, yet significant discrepancies are observed at CM 1 and CM 2 in X and Y-directions, with errors exceeding 1 mm. These deviations partly stem from local warpage, asymmetric shrinkage, and geometric features such as sharp transitions that are not fully captured by the sim-

ulation. Additional geometric phenomena, such as seam lines and material bulges, are also observed in the XCT data, further emphasising the complexity of sintering-induced deformation in metal FFF parts. The results underscore the need for improved representative predictive models and design guidelines for metal FFF, particularly when manufacturing functionally critical geometries.

Future work will explore integrating data-driven learning models with simulation to improve the prediction of local geometric deviations and guide compensation strategies. The proposed XCT-based framework provides a robust foundation for data-driven quality assurance and model validation in metal additive manufacturing workflows.

Acknowledgments

This work was carried out at the University of Cambridge, Institute for Manufacturing, Computer Aided Manufacturing Group in the UK, in collaboration with Chalmers University of Technology, Sweden. This work is supported by the Swedish Innovation Agency (VINNOVA), project 2024-03565. The support is gratefully acknowledged.

Conflicts of interest

SWP is a co-founder of Matta Labs, a company selling AI systems to manufacturers. CM is a part-time intern at Matta Labs.

References

[1] J. Beaman, D. L. Bourell, C. Seepersad, D. Kovar, Additive manufacturing review: early past to current practice, Journal of Manufacturing Science and Engineering 142 (11) (2020) 110812.
[2] M. Ziaee, N. B. Crane, Binder jetting: A review of process, materials, and methods, Additive Manufacturing 28 (2019) 781–801.
[3] D.-G. Ahn, Directed energy deposition (ded) process: state of the art, International Journal of Precision Engineering and Manufacturing-Green Technology 8 (2) (2021) 703–742.
[4] O. A. Mohamed, S. H. Masood, J. L. Bhowmik, Optimization of fused deposition modeling process parameters: a review of current research and future prospects, Advances in manufacturing 3 (2015) 42–53.
[5] S. Sun, M. Brandt, M. Easton, Powder bed fusion processes: An overview, Laser additive manufacturing (2017) 55–77.
[6] S. A. Tofail, E. P. Koumoulos, A. Bandyopadhyay, S. Bose, L. O'Donoghue, C. Charitidis, Additive manufacturing: scientific and technological challenges, market uptake and opportunities, Materials today 21 (1) (2018) 22–37.
[7] R. S. Tabar, A. Lindkvist, L. Lindkvist, K. Wärmefjord, R. Söderberg, Fixture layout optimization for remanufacturing using directed energy deposition process, Procedia CIRP 129 (2024) 199–204.
[8] S. Singh, G. Singh, C. Prakash, S. Ramakrishna, Current status and future directions of fused filament fabrication, Journal of Manufacturing Processes 55 (2020) 288–306.
[9] D. A. Brion, S. W. Pattinson, Generalisable 3d printing error detection and correction via multi-head neural networks, Nature communications 13 (1) (2022) 4654.
[10] E. Ferraris, J. Zhang, B. Van Hooreweder, Thermography based in-process monitoring of fused filament fabrication of polymeric parts, CIRP Annals 68 (1) (2019) 213–216.
[11] J. Zhang, J. Neeckx, J. Troukens, E. Ferraris, A reheating temperature criterion for adaptive strategy in fused filament fabrication, CIRP Annals 71 (1) (2022) 197–200.
[12] Y. Thompson, J. Gonzalez-Gutierrez, C. Kukla, P. Felfer, Fused filament fabrication, debinding and sintering as a low cost additive manufacturing method of 316l stainless steel, Additive Manufacturing 30 (2019) 100861.
[13] M. Sadaf, M. Bragaglia, F. Nanni, A simple route for additive manufacturing of 316l stainless steel via fused filament fabrication, Journal of Manufacturing Processes 67 (2021) 141–150.
[14] J. Jacob, D. Pejak Simunec, A. E. Kandjani, A. Trinchi, A. Sola, A review of fused filament fabrication of metal parts (metal fff): Current developments and future challenges, Technologies 12 (12) (2024) 267.
[15] F. Léonard, S. Tammas-Williams, Metal fff sintering shrinkage rate measurements by x-ray computed tomography, Nondestructive Testing and Evaluation 37 (5) (2022) 631–644.
[16] D. Jiang, F. Ning, Anisotropic deformation of 316l stainless steel overhang structures built by material extrusion based additive manufacturing, Additive Manufacturing 50 (2022) 102545.
[17] I. Ait-Mansour, N. Kretzschmar, S. Chekurov, M. Salmi, J. Rech, Design-dependent shrinkage compensation modeling and mechanical property targeting of metal fff, Progress in Additive Manufacturing 5 (2020) 51–57.
[18] J. E. Montes-Ramirez, A. Lopez, M. S. Hassan, J. Munoz, S. Arroyo, C. Marquez, S. Zaman, A. Nunez, M. S. Mahmud, A. Gandara, et al., Shrinkage and deformation compensation in metal fused filament fabrication (mf3) sintered copper components using 3d scanning and inverse deformation, Journal of Manufacturing Processes 121 (2024) 9–19.
[19] R. S. Tabar, R. Söderberg, D. Ceglarek, P. Franciosa, L. Lindkvist, Augmented geometry assurance digital twin with physics-based incremental learning, CIRP Annals 74 (1) (2025) 151–155.
[20] R. Sadeghi Tabar, L. Lindkvist, K. Wärmefjord, P. Franciosa, D. Ceglarek, R. Söderberg, Enhancing welding geometric precision: analyzing the impact of weld path directions, sequences and locating schemes on displacement, Applied Sciences 14 (23) (2024) 11144.
[21] R. Sadeghi Tabar, H. Zheng, F. Litwa, K. Paetzold-Byhain, L. Lindkvist, K. Wärmefjord, R. Söderberg, Digital twin-based clamping sequence analysis and optimization for improved geometric quality, Applied Sciences 14 (2) (2024) 510.
[22] Forward AM, Ultrafuse® 316l, stainless steel composite metal filament for 3d printers, Accessed 2025-07-10.
URL https://forward-am.com/material-portfolio/ultrafuse-filaments-for-fused-filaments-fabrication-fff/metal-filaments/ultrafuse-316l/
[23] A. Fedorov, R. Beichel, J. Kalpathy-Cramer, J. Finet, J.-C. Fillion-Robin, S. Pujol, C. Bauer, D. Jennings, F. Fennessy, M. Sonka, et al., 3d slicer as an image computing platform for the quantitative imaging network, Magnetic resonance imaging 30 (9) (2012) 1323–1341.
[24] CloudCompare (version 2.13) , [gpl software], Accessed 2025-07-10.
URL http://www.cloudcompare.org/